Mathematical Biosciences and Engineering

MBE, 20(9): 17138–17157.
DOI: 10.3934/mbe.2023764
Received: 10 July 2023
Revised: 12 August 2023
Accepted: 21 August 2023
Published: 04 September 2023

http://www.aimspress.com/journal/MBE

Research article

Improved graph neural network-based green anaconda optimization for segmenting and classifying the lung cancer

S. Dinesh Krishnan[1], Danilo Pelusi [2], A. Daniel[3,*], V. Suresh[4] and Balamurugan Balusamy[5]

[1] Assistant professor, B V Raju Institute of Technology, Narsapur, Telangana, India
[2] Department of Communication Sciences, University of Teramo, Italy
[3] Associate Professor, Amity University, Gwalior, Madhya Pradesh, India
[4] Assistant professor, Dr. N. G. P Institute of Technology, Coimbatore, India
[5] Associate Dean-Student Engagement, Shiv Nadar University, India

* **Correspondence:** Email: danielarockiam@gmail.com; Tel: +919786843789.

Abstract: Normal lung cells incur genetic damage over time, which causes unchecked cell growth and ultimately leads to lung cancer. Nearly 85% of lung cancer cases are caused by smoking, but there exists factual evidence that beta-carotene supplements and arsenic in water may raise the risk of developing the illness. Asbestos, polycyclic aromatic hydrocarbons, arsenic, radon gas, nickel, chromium and hereditary factors represent various lung cancer-causing agents. Therefore, deep learning approaches are employed to quicken the crucial procedure of diagnosing lung cancer. The effectiveness of these methods has increased when used to examine cancer histopathology slides. Initially, the data is gathered from the standard benchmark dataset. Further, the pre-processing of the collected images is accomplished using the Gabor filter method. The segmentation of these pre-processed images is done through the modified expectation maximization (MEM) algorithm method. Next, using the histogram of oriented gradient (HOG) scheme, the features are extracted from these segmented images. Finally, the classification of lung cancer is performed by the improved graph neural network (IGNN), where the parameter optimization of graph neural network (GNN) is done by the green anaconda optimization (GAO) algorithm in order to derive the accuracy maximization as the major objective function. This IGNN classifies lung cancer into normal, adeno carcinoma and squamous cell carcinoma as the final output. On comparison with existing methods with respect to distinct performance measures, the simulation findings reveal the betterment of the introduced method.

Keywords: lung cancer segmentation; lung cancer classification; Improved Graph Neural Network; Green Anaconda Optimization

Abbreviations: MEM: Modified Expectation Maximization; SCLC: Small Cell Lung Cancer; HOG: Histogram of Oriented Gradient; NSCLC: Non-Small Cell Lung Cancer; IGNN: Improved Graph Neural Network; E: Eosin; GAO: Green Anaconda Optimization; H: Hematoxylin; mRFCN: multidimensional Region-based Fully Convolutional Network; CNN: Convolutional Neural Network; mLRPN: multi-Layer fusion Region Proposal Network; AUC: Area-Under-Curve; 3-D: three-dimensional; BN: Batch Normalization; RoI: Region of Interest; LUNA16: LUng Nodule Analysis 2016; LUSC: LUng Squamous cell Carcinoma; Kaggle DSB 2017: KAGGLE DATA-SCIENCE-BOWL-2017; ASC: Adeno Squamous Carcinoma; CT: Computerized Tomography; ROC: Receiver Operating Characteristic; E-DBN: Enhanced Deep Belief Network; SVMs: Support Vector machines; GB: Gaussian-Bernoulli; ML: Machine Learning; BB: Bernoulli-Bernoulli; SSSO-based MORAN: Shuffled Social Sky Optimizer-based Multi-Object Rectified Attention Network; FNR: False Negative Rate; SSD: Social Ski-Driver; FPR: False Positive Rate; SSOA: Shuffled Shepherd Optimization Algorithm; CapsNet: Capsule Neural Network; DREFC: Deep Renyi Entropy Fuzzy Clustering; LIDC: Lung Image Database Consortium; GLCM: Gray-Level Co-occurrence Matrix; FCM: Fuzzy C-Means; LGXP: Local Gabor XOR Pattern; ECM-CSD: Efficient Classification Model for Cancer Stage Diagnosis; GBP: Global Binary Pattern; DFCV: Data, Feature Selection, Classification Technique, and View; ALbAE: Ant Lion-based AutoEncoders; MLP: Multi-Layer Perceptron; RF: Random Forest; ELM: Extreme Learning Machine; GTGM: Generative Text-Guided 3D Vision-Language Pre training for Unified Medical Image Segmentation; Med-UniC: Unifying Cross-Lingual Medical Vision-Language Pre-Training; LLM: Large Language Models; CTR: Cross-lingual Text Alignment Regularization.

1. Introduction

The unregulated proliferation of aberrant pulmonary cells represents a symptom of lung cancer. According to histology, prognosis, biological behavior and therapy, there are two main forms of lung cancer [1]. SCLC and NSCLC represent the two types [2]. NSCLC makes up 85% of cases and SCLC accounts for the other 15%. The most prevalent kind of NSCLC, adenocarcinoma, develops in epithelial cells that exude mucus or fluids [3]. Squamous cells that line several organs, including the bladder, lung, intestines, kidney, and stomach, are where squamous cell carcinoma develops [4].

Lung cancer may be diagnosed using a number of techniques, including CT scans, X-rays, bronchoscopies, PET-CT scans and biopsies [5]. H and E staining, in which the staining is performed on the tissue extracted from a biopsy, is commonly utilized to determine the subtype of lung cancer on the basis of the tissue type. E includes a pink color and stains proteins, whereas H involves a deep purple color and stains nucleic acids in cells [6]. According to research, lung cancer therapy as well as survival are related to the kind of histology [7]. Recent developments in genetic research have cleared the way for personalized treatment for people with lung cancer [8].

It is also crucial to analyze the histopathological images of the disease [9]. Manually analyzing histopathology results, nevertheless, takes time and is not objective. Pathologists are struggling to handle the burden associated with histopathologic cancer detection [10]. In order to lessen the workload on pathologists and accelerate the crucial procedure of lung cancer detection, deep learning

approaches are employed [11]. The effectiveness of these methods has increased when used to examine cancer histopathology slides.

The paper contribution is as follows:

- To employ a deep learning approach to quicken the crucial procedure of diagnosing lung cancer.
- To accomplish the pre-processing of the collected images using Gabor filter method.
- To do the segmentation of the pre-processed images through the MEM algorithm method.
- To extract the features from the segmented images using the HOG scheme.
- To perform the classification of the lung cancer by the IGNN, where the parameter optimization of GNN is done by the GAO in order to derive the accuracy maximization as the major objective function.
- To classify the lung cancer into normal, adenocarcinoma and squamous cell carcinoma as the final output by the IGNN.

The paper organization is as follows: Section 1 is the introduction of the lung cancer classification model. Section 2 is a literature survey about it. Section 3 is the proposed methodology in consideration of the IGNN and GAO algorithms. Section 4 shows the results in detail for the lung cancer classification model. Section 5 ends with the conclusion.

2. Related work

In 2020, Masood et al. [12] suggested an improved mRFCN-based lung nodule identification as well as classification. We used a median intensity extension to make use of the 3-D data and we included a deconvolutional layer to incorporate the suggested mLRPN in the framework to choose the possible RoI. The simulation findings demonstrated good detection efficiency in compared to the conventional nodule detection/categorization approaches. The framework was trained and tested utilizing the LIDC dataset.

In 2020, Bicakci et al. [13] thoroughly examined deep learning-oriented classification techniques to distinguish between the two NSCLC subtypes known as squamous cell carcinoma and adenocarcinoma. 38 slices were of patients having ADC, while the remaining slices were of SqCC patients. To investigate the impact of peritumoral regions in PET scans on the subtype categorization of tumors, three trials were conducted. In these simulations, we evaluated three CNN methods, including VGG16, SqueezeNet, and VGG19, employing three different types of images: entire slices without segmentation or cropping, square subimages cropped to involve the tumor and random walk technique segmented image parts respective to tumors. Every method was optimized for the diagnostic categorization using a variety of optimizers and regularization techniques. F-score and AUC measures were employed to assess the effectiveness of the project. The findings allow us to conclude that peritumoral areas and tissues are both required for the development of methods and eliminate the need for segmentation.

In 2021, Chen et al. [14] suggested LDNNET, which incorporated Dense-Block, dropout and BN. LDNNET, an adaptable framework on the basis of convnets incorporating softmax classifier, was used to address the issues with deep convnet training. The primary work is as below: First, we classified lung nodules using the database LDNNET on LUNA16, and lung cancers using the database Kaggle DSB 2017. Second, the comparative tests were made to assess how well lung CT images with thick connections, pooling layers and larger input pixels operate. Third, LDNNET used dense connection, dropout layer and data augmentation to minimize overfitting. Fourth, to examine

the pre-processing on the categorization of images, several pre-processing techniques were contrasted to the no-processing technique. Fifth, the indices of specificity, accuracy and sensitivity on LUNA16 were 0.994585, 0.988396 and 0.982072, respectively, while they were 0.999652, 0.999480 and 0.998974 on Kaggle DSB 2017. Additionally, the AUC for the two datasets was greater than 0.98. Since lung images were used as input images without any preprocessing, this research runs simulations to demonstrate that LDNNET was still the more enhanced method compared to various existing methods. Additionally, a number of comparison tests were carried out to further demonstrate, via verification and discussion, that the suggested method has superior accuracy and resilience.

In 2021, Li et al. [15] involved very uncommon lung adenosquamous carcinoma specimens for the initial time. The relief method was utilized after the multidimensional characteristics of 121 LC histopathology images were initially retrieved. The ROC curve and AUC were utilized to more easily assess the classifier's capacity for generalization while the SVMs classifier was employed to categorize LC subtypes. Lastly, investigations demonstrate that the Relief-SVM method achieves the optimal classification impact via a horizontal comparison with a range of widely used classification methods. The accuracy of the classifications using the LUSC-SCLC, LUSC-ASC and ASC-SCLC systems was 83.91%, 73.91% and 73.67%, respectively. The effectiveness of the auxiliary diagnosis method created by ML in the detection of LC is confirmed by the simulation findings.

In 2023, Ahmad et al. [16] suggested a fresh approach to categorizing lung CT scans. We combine Gabor filters with an E-DBN and several classification techniques in the suggested strategy for classifying lung cancer. We employ the GB and BB RBMs as two cascaded RBMs in this E-DBN. Of all the applicable approaches, a SVM provides the optimal performance metrics.

In 2022, Ajni and Anitha [17] created a technique known as SSSO-based MORAN to accurately categorize lung cancer illness. The SSD algorithm and the SSOA have been combined to create the SSSO algorithm. The pre-processing stage receives the input CT image, which is then used to pre-process the image using Gaussian filtering. As a result, the input image's RoI was obtained. After that, the suggested DREFC is used to segment the lung lobes. The nodule region was recognized from the lung image using the segmented lung lobes, and cancer was classified on the basis of characteristics. GLCM features, LGXP, Tetrolet transform, GBP and statistical characteristics were among the features taken into account.

In 2023, Bushara et al. [18] put forth a brand-new deep learning methodology referred as LCD-CapsNet to reduce the enormous quantity of information and attain spatial invariance for lung cancer detection. The main goal of the suggested approach was to construct methods that would categorize and analyze images. This deep learning methodology was evaluated using the LIDC datasets.

In 2019, Kavitha et al. [19] suggested a region-oriented FCM clustering method, which significantly improves mortality in clinical practice. CT lung images are used for processing in the developed ECM-CSD, because they offer greater imaging resolution, sensitivity, and excellent isotopic collection in lung nodule detection. These images have undergone pre-processing using a Gabor filter for enhancing and a Gaussian filter for smoothing. Next, utilizing FCM-oriented clustering, an efficient segmentation of lung nodules was carried out on the basis of the retrieved image characteristics. The SVM classification method is often used to determine the phases of cancer. Additionally, the method was examined using the MATLAB platform and the clinical dataset of LIDC-IDRI lung CT scans. The comparison studies demonstrate the suggested method's effectiveness with respect to performance assessment parameters such as improved accuracy and decreased error rate.

In 2023, Alsadoon et al. [20] looked into, found and carefully examined DL methods that

performed well in the categorization of lung cancer. 37 articles out of the 338 we assessed satisfied the requirements for consideration in the suggested paradigm. In addition, we provide and assess a structure to control the procedure for choosing and deploying DL methods in actual systems. DFCV are the framework's four primary parts. On the basis of 37 cutting-edge research publications, we examine the effectiveness and significance of the developed DFCV method. The DFCV framework could serve as a manual for choosing and implementing DL-oriented solutions in lung cancer treatment facilities.

In 2023, Braveen et al. [21] put up a unique ALbAE method for accurate lung cancer and pneumonia categorization. Initially, noise artefacts were removed from CT images employing median filters to enhance the image quality. Therefore, the ALbAE approach is used to extract the pertinent characteristics, like pixel rates, image edges and blood clots. Lastly, utilizing the RF approach, the lung CT scans were divided into three groups, including lung affected by malignancy, normal lung and lung impacted by pneumonia. Distinct metrics, including recall, accuracy, precision and F1-measure, are used to determine how successful the executed methodology was. The created methodology achieves 98% recall as well as F-measure rate, whereas the developed methodology achieves 96% precision score. The developed technique achieves 97% accuracy. According to simulation results, the suggested methodology was more accurate at identifying pneumonia and lung cancer than the ELM, SVM and MLP models that are already in use.

In 2023, Chen et al. [22] proposed a methodology that extended VLP to 3D medical images without depending on associated textual descriptions called GTGM. LLM are specifically used by GTGM to produce medical-style text from 3D medical images. The learning of 3D visual representations was next supervised using this synthetic text. In order to foster consistent visual descriptions amongst enhanced 3D medical image patches, a negative-free contrastive learning goal technique was also implemented, which successfully reduces the biases linked with strict positive-negative sample pairings. The GTGM was tested on 13 datasets from MRI, CT and EM, three imaging modalities. As a result of facilitating VLP expansion into 3D medical imagery without the requirement for associated text, GTGM's exceptional efficiency across a variety of medical image segmentation tasks highlights its efficacy and adaptability.

In 2023, Qin et al. [23] extensively investigated the knowledge transferability associated with pre-trained VLMs to the medical area, in which it was demonstrated that the key to eliciting information from pre-trained VLMs is to use well-modelled medical cues. It was shown that the VLM could transport the knowledge across domains and enhance its generalization by suggesting with expressive features that were shared across domains. The ability to recognize novel things with fewer or no image specimens was provided by this process. In addition, three methods were studied for automatic development of medical cues that may use expert level medical knowledge and image-specific data for fine-grained grounding in order to bypass the time-consuming human modelling procedure. We undertake comprehensive studies on thirteen distinct medical datasets spanning a variety of modalities, demonstrating that the carefully crafted cues significantly outperform the standardized cues in terms of zero-shot effectiveness.

In 2023, Wan et al. [24] introduced a revolutionary system called Med-UniC, which aims to combine multimodal medical information from the two major common languages, Spanish and English. To particularly unify cross-lingual semantic descriptions of medical reports coming from several language groups, CTR was developed. By making the optimization aim independent of negative specimens, latent language disentanglement was able to maximize CTR while greatly reducing the

bias that results from identifying positive-negative specimen pairings among comparable medical reports. Additionally, it makes sure that no particular language community was overrepresented in the cross-lingual description. Med-UniC provides a flexible methodology for combining multi-modal medical information across many language groups. It achieves exceptional effectiveness across five medical imaging tasks and ten datasets covering more than thirty disorders. The results linked with the simulation demonstrate the existence of community bias in cross-lingual VLP. The effectiveness of both uni-modal visual tasks and vision-language was improved by minimizing this bias.

3. Proposed methodology

The proposed lung cancer classification model includes various phases such as data gathering, pre-processing, segmentation, feature extraction and classification. The common benchmark dataset is where the data is initially acquired. Additionally, the acquired images are pre-processed utilizing the Gabor filter technique. These pre-processed images are segmented via the MEM algorithm technique. The characteristics are then retrieved from these segmented images employing the HOG technique. The IGNN is used to classify lung cancer, and the GAO method is used to optimize the parameters of the GNN in order to maximize accuracy as the main objective function. The final output of this IGNN categorizes lung cancer as normal, adenocarcinoma and squamous cell carcinoma. The overall model of the developed lung cancer classification is shown in Figure 1.

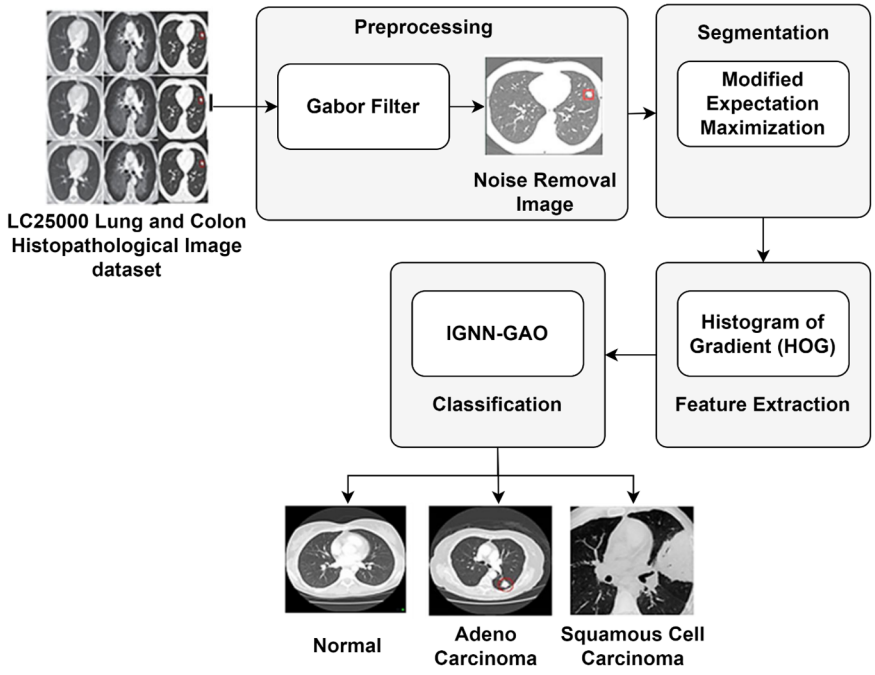

Figure 1. Overall model of the developed lung cancer classification.

3.1. Data collection

The LC25000 Lung and Colon Histopathological Image collection, which includes 5000 images in each among the three groups of benign (normal cells), squamous and adenocarcinoma carcinoma

cells (both malignant cells), is where the data is taken from. The dataset has been verified and is HIPAA appropriate. By rotating left as well as right and flipping horizontally and vertically, augmentation is accomplished.

3.2. Pre-processing

The pre-processing for the lung cancer classification model is accomplished by the Gabor filter method. Owing to its localization in the spatial as well as spatial frequency domains, it may be characterized as a Gaussian modulated sinusoid. A 2-D sinusoidal plane wave having orientation θ as well as radial center frequency g_0 modulated by a Gaussian envelope containing standard deviations σ_x and σ_y correspondingly along the x and y axes has the real impulse response provided by:

$$i(y,z) = \frac{1}{2\pi\sigma_x\sigma_y} exp\left\{-\frac{1}{2}\left[\frac{x^2}{\sigma_x^2} + \frac{y^2}{\sigma_y^2}\right]\right\} cos(2\pi g_0 x). \quad (1)$$

Here, $x = x\,cos\,cos\,\theta + y\,sin\,sin\,\theta$ and $y = -x\,sin\,sin\,\theta + y\,cos\,cos\,\theta$. The Gabor filter should be described as two symmetrically spaced Gaussians in the relevant spatial-frequency domain as shown.

$$I(u,v) = exp\{-2\pi^2[(u-g_0)^2\sigma_x^2 + v^2\sigma_y^2]\} + exp\{-2\pi^2[(u+g_0)^2\sigma_x^2 + v^2\sigma_y^2]\}. \quad (2)$$

After establishing the frequency cut-off as -6 db and the frequency and orientation bandwidths (C_g, C_θ) to constant values corresponding to psycho visual information, the Gaussian envelope unknowns σ_x and σ_y may be calculated as in Eq (3). The optimum distance among the radial frequencies is specifically one octave. The octave-specified frequency bandwidth (i.e., the distance among g_1 and its double g_2) grows in a logarithmic manner as indicated by $\left(\frac{g_2}{g_1}\right)$. This was motivated by research that revealed basic cells in the visual cortex had a frequency bandwidth of around one octave. A circular Gaussian with equal spatial coverage in all directions and a 45° orientation bandwidth was selected for this experiment by setting $\sigma_x = \sigma_y$.

$$\sigma_x = \frac{\sqrt{ln2}(2^{C_g}+1)}{\sqrt{2\pi}g_0(2^{C_g}-1)} \quad \sigma_x = \frac{\sqrt{ln2}}{\sqrt{2\pi}g_0 tantan\left(\frac{C_\theta}{2}\right)}. \quad (3)$$

The influence of aliasing should be lessened, and data should be properly captured with precise filter characteristic tuning. This is accomplished by choosing the filter location (g_0, θ) and bandwidth (σ_x, σ_y) appropriately. Additionally, it is important to ensure that the channel filters' core frequencies are near to the frequencies that are typical in order to avoid the filter response falling off too quickly. Overall, $B \times \left(\frac{O_d}{2}\right)$, in which O_d shows the image width and B shows the count of orientation separations, gives the quantity of dyadic Gabor filter banks needed.

The process of employing a number of banks is similar to how the scaling function and mother wavelet are scaled and converted for the development. The basis created by the Gabor function is non-orthogonal and results in redundant decompositions, yet it is nonetheless accepted as an acceptable

wavelet. Additionally, the count of needed frequencies for locating the centers must be set beforehand on the basis of the size of the converted image, in a manner identical to determining the count of decomposition stages for the wavelet packets.

The energy $F_l, l = 1, 2$, in which N and O represents the size of the subband intensity $J_g(x, y)$, shows the traditional approach for extracting the Gabor filter signature.

$$F_l = \frac{1}{NO}\sum_{y=0}^{N-1}\sum_{x=0}^{O-1}\left|J_g(x, y)\right|^l. \tag{4}$$

3.3. Segmentation

The segmentation is performed by the Modified Expectation Maximization (MEM) [25] method for the developed lung cancer classification model. The weights used in the MEM method determine how closely the estimated value is connected to each segment of the separated component. A replicated matrix is used to compare single pixel to another in order to calculate the concealed information. In comparison to various procedures, the segmentation outcome is therefore more appropriate.

Stages in the MEM algorithm are as follows: Initialize the settings for the expectation and maximization steps first. The maximization will next be increased by one stage. Concatenating the supplied image represents the following stage. Swap out the matrices for expectation and maximization. Find the differences between the input image and the duplicated image. Determine the novel expectation and stage location for maximization. Reiterate the expectation and stage value maximization.

3.4. Feature extraction

The features are gathered from the segmented images of the developed lung cancer classification model utilizing the HOG scheme. In order to extract typical features from the segmented images, the HOG scheme is investigated. The image is initially partitioned into cells for the purpose of implementing HOG, after which the HOG orientations for the pixels inside the cells are generated. To describe the image description, the resultant histograms are next concatenated. Nevertheless, local histograms are contrast normalized by measuring an intensity metric across a wider portion of the image known as a block, which improves the effectiveness of the descriptor. The block's cells are next completely normalized based on their intensity values, creating a description that is more resistant to variations in lighting and shadows. To measure HOG, there exists four main phases.

The input image J is filtered through the kernels in both the horizontal and vertical directions employing the 1D derivative mask.

$$E_x = [-1\ 0\ 1\ ]\ E_y = [1\ 0\ -1\ ]^T. \tag{5}$$

Here, a transposition vector $[\cdot]^T$ is used. The convolution process is next used to derive the x and y derivatives of the grayscale or silhouette image J as

$$J_x = J * E_x\ J_y = J * E_y. \tag{6}$$

The below formulas are used to calculate the gradient of J's magnitude as well as direction, accordingly:

$$|H| = \sqrt{J_x^2 + J_y^2}, \tag{7}$$

$$\theta = arctan\left(\frac{J_y}{J_x}\right). \tag{8}$$

A process known as orientation binning, which requires the production of cell histograms, represents the second stage in the calculation of HOG. The histogram channels for HOG are either signed or unsigned, and the HOG cells are rectangular (or circular in certain genuine applications). Unsigned channels in a histogram are scattered over a range of 0 to 360 degrees, whereas signed channels are distributed over a range of 0 to 180 degrees.

Descriptor block formation represents the third phase in the HOG computing process. This process is used to take variations in lighting and contrast into consideration. Half the size of a block's worth of blocks are positioned on top of one another.

Block normalization represents the last stage of the HOG calculation. One among the below norms serves as the normalization factor for a nonnormalized vector (w) that includes the histogram in a particular block:

$$l2\ norm: g = \frac{w}{\sqrt{\|w\|_2^2 + f^2}}\ l1\ norm: g = \frac{w}{\|w\|_1 + f}\ l1\ sqrt: g = \sqrt{\frac{w}{\|w\|_1 + f}}. \tag{9}$$

Here, f shows a constant whose value has no bearing on the outcome. Here, the size, shape and position of the lung cancer is mostly considered as extracted features for the classification of lung cancer.

3.5. Classification by IGNN

The classification of the developed lung cancer model is accomplished by the IGNN model. Here, the parameters of GNN are tuned by green anaconda optimization (GAO) in order to enhance the classification performance as well as to derive the fitness function. Adjacency matrix B, the Laplacian M, or their normalized variants are examples of GNN $T \in S^{O \times O}$ that illustrate the sparsity as well as connectedness of a graph H. The GNNs are symmetric because we limit the graph to being unweighted and undirected. Signals may be moved and averaged throughout their neighborhoods employing GNN. The graph signal's single time shift is denoted by Ty, and its value at node w_j is $[Ty]_j = \sum_{k|(w_k,w_j)\in\varepsilon} t_{jk} y_k$. Utilizing polynomials of GNN and the filter weights $i = \{i_l\}_{l=0}^{L}$ in the graph convolutional filter, $i(T)$ having $L+1$ taps is created.

$$z = i_0 T^0 y + i_1 T^1 y + \cdots + i_L T^L y = i(T) y. \tag{10}$$

Here, $i(T) = [i_0 T^0, i_1 T^1, \cdots, i_L T^L]$ signifies the weight of local data following L-hop information exchanges and describes a shift-invariant graph filter having $L+1$ taps.

Layers of graph convolutional filters are accompanied by nonlinearities in a generic GNN. The input graph signal having e features is denoted by matrix Y, where $Y = [y_1, \cdots, y_e]$, and the feature propagation in a single GNN layer is represented as

$$Z = \sigma\left(\sum_{l=0}^{L} T^l Y I_l\right). \tag{11}$$

Here, D shows the count of output features, $I_l \in S^{e \times D}$ shows the collection of the l^{th} entries of the $e \times D$ learnable graph filters, and σ signifies the pointwise nonlinear activation function.

3.6. GAO Algorithm

The GAO is selected to perform the parameter tuning in GNN with the intention of enhancing the performance of classification thereby attaining the appropriate objective function. The GAO mimics green anaconda behavior in its native state. The process used by male species to locate female species during the breeding season as well as the green anaconda's hunting method served as the foundation for GAO. On the basis of the simulation of these two green anaconda strategy stages of exploration as well as exploitation, GAO's analytical modelling is provided.

A population-oriented metaheuristic algorithm, the developed GAO includes green anacondas as members of its population. Equation (13) is used to randomly create every green anaconda's starting location within the search space before the method is run.

$$Y = \left[Y_1 \vdots Y_j \vdots Y_O\right]_{O\times n} = \left[y_{1,1} \cdots y_{1,e} \cdots y_{1,n} \vdots \ddots \vdots \therefore \vdots y_{j,1} \cdots y_{j,e} \cdots y_{j,n} \vdots \therefore \vdots \ddots \vdots y_{O,1} \cdots y_{O,e} \cdots y_{O,n}\right]_{O\times n}. \quad (12)$$

$$y_{j,e} = lb_e + s_{j,e} \cdot (ub_e - lb_e), j = 1, 2, \cdots, O, e = 1, 2, \cdots, n. \quad (13)$$

Here, Y shows the GAO population matrix, Y_j represents the j^{th} green anaconda (possible solution), $y_{j,e}$ represents the search space's thickness in e^{th} dimension (decision variable), number of green anacondas are referred to as O, decision variables as n, random numbers as $s_{j,e}$ and lower and upper bounds of the e^{th} decision variable as lb_e and ub_e, correspondingly.

The objective function of the issue may be assessed in accordance with the recommended values associated with every green anaconda for the choice variables. According to Eq (14), a vector may be used to mathematically describe this collection of determined values for the goal function.

$$G = \left[G_1 \vdots G_j \vdots G_O\right]_{O\times 1} = \left[G(Y_1) \vdots G\left(Y_j\right) \vdots G(Y_O)\right]_{O\times 1}. \quad (14)$$

Here, G_j shows the computed objective function on the basis of the j^{th} green anaconda and G shows the vector related to the computed objective function.

Equation (15) is used to identify the group of possible female species for every green anaconda.

$$DGM^j = \left\{Y_{l_j}: G_{l_j} < G_j \text{ and } l_j \neq j\right\}, where\ j = 1, 2, \cdots, O \text{ and } l_j \in \{1, 2, \cdots, O\}. \quad (15)$$

Here, l_j shows the green anaconda row count in the GAO population matrix and the position count of the respective element in the objective function vector that involves a better objective function value than the j^{th} green anaconda, and DGM^j shows the group of candidate females' positions for the j^{th} green anaconda.

The motion of green anacondas is significantly influenced by the pheromone content. The values of the goal function have been utilized to replicate the pheromone intensity. As a result, the likelihood that a member will be chosen by the green anaconda increases with the value of that member's goal function.

$$QD_k^j = \frac{DGG_k^j - DGG_{max}^j}{\sum_{o=1}^{o_j} DGG_o^j - DGG_{max}^j}, where\ j = 1, 2, \cdots, O\ and\ k = 1, 2, \cdots, o_j. \quad (16)$$

Here, DGG^j shows the vector related to the group of objective function values of candidate females for the j^{th} green anaconda, DGG_k^j shows its k^{th} value, DGG_{max}^j shows its maximum value, and o_j shows the count of candidate females for the j^{th} green anaconda. QD_k^j shows the probability of the pheromone intensity related to the k^{th} female for the j^{th} green anaconda.

Equation (17) is to replicate this selection procedure. Equation (18) next determines the chosen female species for the green anaconda.

$$D_k^j = QD_k^j + D_{k-1}^j, where\ j = 1, 2, \cdots, O, k = 1, 2, \cdots, n, and\ D_0^j = 0. \quad (17)$$

$$TG^j = DGM_k^j : D_{k-1}^j < s_{j,k} < D_k^j. \quad (18)$$

Here, TG^j represents the chosen female for the j^{th} green anaconda, D_k^j shows the cumulative probability function associated with the k^{th} candidate female for the j^{th} green anaconda and s shows a random integer having a normal distribution between [0, 1].

Equation (19) is used to determine a random location after finding the chosen female species. Equation (20), states that the location of the matching green anaconda is modified to the novel location if the goal function's value is better in the novel place; else, it will stay in the old location.

$$y_{j,e}^{Q1} = y_{j,e} + s_{j,e} \cdot \left(TG_e^j - J_{j,e} \cdot y_{j,e}\right), j = 1, 2, \cdots, O, and\ e = 1, 2, \cdots, n. \quad (19)$$

$$Y_j = \{Y_j^{Q1}, G_j^{Q1} < G_j\ \ Y_j, else. \quad (20)$$

O shows the count of green anacondas, n shows the count of decision variables, TG_e^j shows the e^{th} dimension of the chosen female for the j^{th} green anaconda, $J_{j,e}$ represents random numbers from the group $\{1,2\}$, Y_j^{Q1} shows the novel recommended location of the j^{th} green anaconda on the basis of the initial stage of GAO, $y_{j,e}^{Q1}$ shows its e^{th} dimension, G_j^{Q1} shows its objective function value and $s_{j,e}$ represents the random numbers having a normal distribution in [0, 1] range.

Utilizing Eq (21), a random location is initially created next to every green anaconda in relation to the approaching prey. Equation (22), on the other hand, states that it is okay to alter the position of the green anaconda if the goal function's value is enhanced at this novel place.

$$y_{j,e}^{Q2} = y_{j,e} + \left(1 - 2s_{j,e}\right)\frac{ub_e - lb_e}{u}\ j = 1, 2, \cdots, O, e = 1, 2, \cdots, n, and\ u = 1, 2, \cdots, U. \quad (21)$$

$$Y_j = \{Y_j^{Q2}, G_j^{Q2} < G_j \;\; Y_j, else. \tag{22}$$

Here, u shows the algorithm's iteration counter, U shows the maximum count of algorithm iterations, Y_j^{Q2} shows the novel proposed location of the j^{th} green anaconda on the basis of the second stage of GAO, $y_{j,e}^{Q2}$ shows its e^{th} dimension, G_j^{Q2} shows its objective function value, and so forth. In Algorithm 1, many GAO stages are shown as pseudocode.

Algorithm 1: *GAO*

Begin GAO

Input problem data: objective function, variables and constraints of the proposed lung cancer classification model

Place iterations (U) *and GAO population size* (O)

$$y_{j,e} = lb_e + s_{j,e} \cdot (ub_e - lb_e), j = 1, 2, \cdots, O, e = 1, 2, \cdots, n$$

Objective function evaluation of the proposed lung cancer classification model

For $u = 1$ *to* U

For $j = 1$ *to* O

$$DGM^j = \left\{Y_{l_j}: G_{l_j} < G_j \; and \; l_j \neq j\right\}, where \; j = 1, 2, \cdots, O \; and \; l_j \in \{1, 2, \cdots, O\}$$

$$QD_k^j = \frac{DGG_k^j - DGG_{max}^j}{\sum_{o=1}^{o_j} DGG_o^j - DGG_{max}^j}, where \; j = 1, 2, \cdots, O \; and \; k = 1, 2, \cdots, o_j$$

$$D_k^j = QD_k^j + D_{k-1}^j, where \; j = 1, 2, \cdots, O, k = 1, 2, \cdots, n, and \; D_0^j = 0$$

$$TG^j = DGM_k^j: D_{k-1}^j < s_{j,k} < D_k^j$$

$$y_{j,e}^{Q1} = y_{j,e} + s_{j,e} \cdot \left(TG_e^j - J_{j,e} \cdot y_{j,e}\right), j = 1, 2, \cdots, O, and \; e = 1, 2, \cdots, n$$

$$Y_j = \{Y_j^{Q1}, G_j^{Q1} < G_j \;\; Y_j, else$$

$$y_{j,e}^{Q2} = y_{j,e} + \left(1 - 2s_{j,e}\right)\frac{ub_e - lb_e}{u} \; j = 1, 2, \cdots, O, e = 1,2, \cdots, n, and \; u = 1, 2, \cdots, U$$

$$Y_j = \{Y_j^{Q2}, G_j^{Q2} < G_j \;\; Y_j, else$$

End

Save the optimal candidate solution attained so far with the developed lung cancer classification model

End

Output the best quasi-optimal solution attained with the GAO for the developed lung cancer classification model

End GAO

4. Results and discussion

4.1. Experimental setup

The performance rate associated with the introduced strategy may be computed in the results part. Various parameters have been considered for the evaluation of the developed methodology against state-of-the-art works such as MLP [26], SVM [27], ALBAE [21], and ELM [28]. Also, the segmentation algorithm MEM has been compared with conventional techniques such as SV-net [29], self-supervised DL method [30], DREFC [17], IGJO [2], MDE [4], mRSA [6], COVIDOA+HHOA [8], and LCWOA [10]. Better performance has been returned with the proposed model than the other considered works across several iterations. The population size is considered as 10, chromosome length is considered as 1 and the number of iterations is considered as 100. These are the specific parameter settings and optimization strategies utilized for the GAO and IGNN algorithm. The performance of the developed methodology is superior to the other considered state-of-the-art works with respect to different measures.

4.2. Accuracy analysis

Figure 2 and Table 1 show that the suggested IGNN-GAO technique is more accurate than conventional networks like MLP, SVM, ALBAE and ELM. The suggested methodology has a greater accuracy rate when compared to the conventional techniques. As a result, the recommended strategy functions better than conventional techniques. Accuracy in lung cancer categorization refers to the percentage of correctly predicted cases within the input data set. The accuracy formula can be specified as below:

$$accuracy = \frac{tp+tn}{tp+tn+fp+fn}. \tag{23}$$

In the above equation, the terms true positive, true negative, false positive, and false negative are shown by tp, tn, fp and fn, respectively.

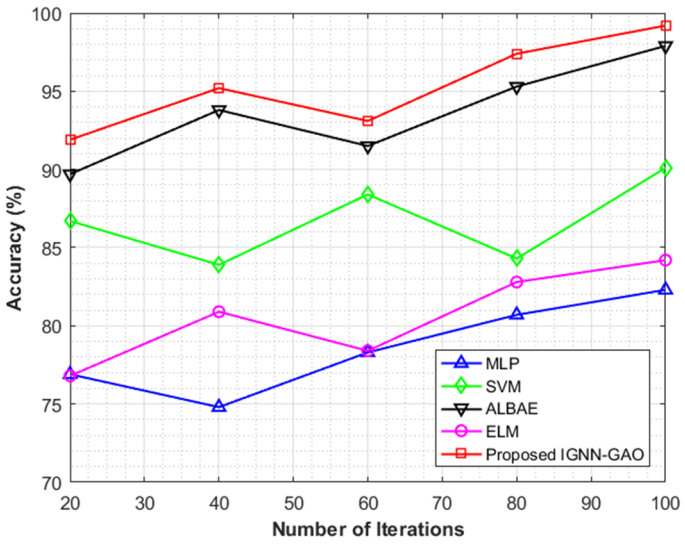

Figure 2. Accuracy analysis.

Table 1. Accuracy analysis.

Methods	Iterations				
	20	40	60	80	100
ALBAE [21]	89.7	93.8	91.5	95.3	97.9
MLP [26]	76.9	74.8	78.3	80.7	82.3
SVM [27]	86.7	83.9	88.4	84.3	90.1
ELM [28]	76.8	80.9	78.4	82.8	84.2
Proposed IGNN-GAO	91.9	95.2	93.1	97.4	99.2

Nevertheless, a system's capacity is determined by its level of accuracy. The count of true and false positives and true and false negatives is used to calculate the accuracy rate. The suggested method's accuracy rate is 99.2%. It suggests that the technology would identify a specific illness more accurately than the conventional techniques.

4.3. Specificity analysis

Figure 3 and Table 2 provide comparison and specificity analysis examples. The suggested IGNN-GAO approach achieves great specificity when compared to remaining conventional approaches. The formula for specificity is given as below:

$$specificity = \frac{tn}{fp+tn}. \tag{24}$$

The suggested method's specificity rate may be evaluated in comparison to several existing methods. The introduced methodology has achieved 93.8% specificity. It shows that the algorithm may categorize lung cancer on the basis of the images that are provided.

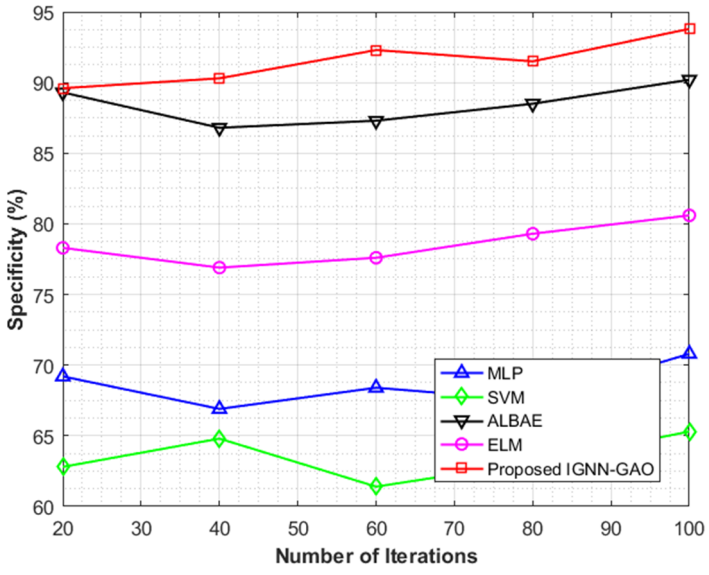

Figure 3. Specificity analysis.

Table 2. Specificity analysis.

Methods	Iterations				
	20	40	60	80	100
ALBAE [21]	89.3	86.8	87.3	88.5	90.2
MLP [26]	69.2	66.9	68.4	67.5	70.8
SVM [27]	62.8	64.8	61.4	63.1	65.3
ELM [28]	78.3	76.9	77.6	79.3	80.6
Proposed IGNN-GAO	89.6	90.3	92.3	91.5	93.8

4.4. Scalability analysis

A system's capacity to scale up or down may be determined by measuring how its effectiveness varies as input size and the number of processors increase. The increase in input size may be caused by one of three objectives: retaining a certain execution time, employing all available memory or handling a predetermined effectiveness. The Figure 4 and Table 3 below exhibit the scalability study of the introduced IGNN-GAO and the cutting-edge techniques.

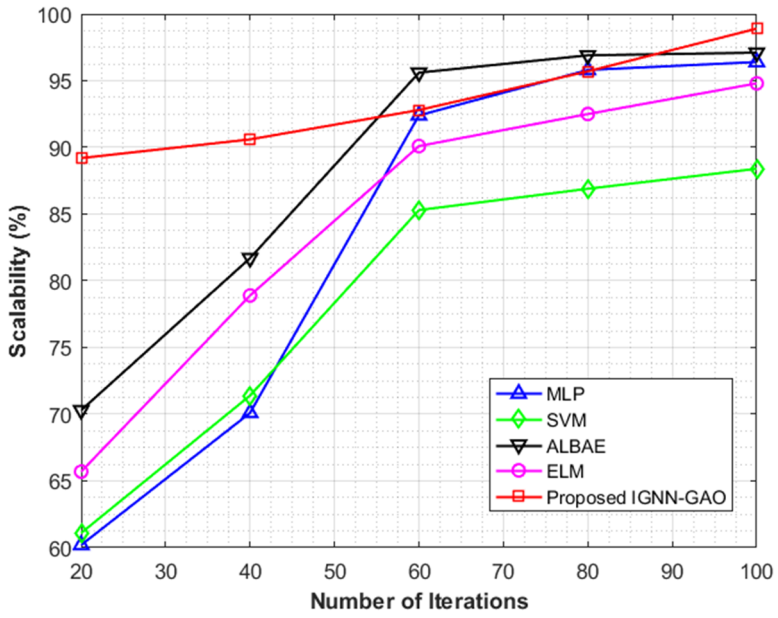

Figure 4. Scalability analysis.

Table 3. Scalability analysis.

Methods	Iterations				
	20	40	60	80	100
ALBAE [21]	70.3	81.7	95.6	96.9	97.1
MLP [26]	60.2	70.1	92.4	95.8	96.4
SVM [27]	61.1	71.4	85.3	86.9	88.4
ELM [28]	65.7	78.9	90.1	92.5	94.8
Proposed IGNN-GAO	89.2	90.6	92.8	95.7	98.9

4.5. Run time analysis

Theoretically, run-time analysis predicts and forecasts how much an algorithm's running time (or execution time) will rise as the size of its input increases. Figure 5 and Table 4 serve as comparison and runtime analysis examples. The suggested IGNN-GAO approach achieves minimal runtime compared to remaining conventional methods.

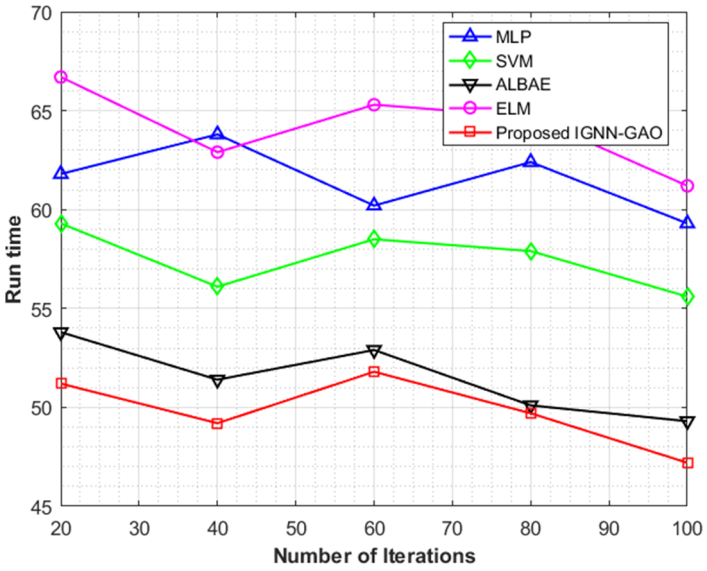

Figure 5. Run time analysis.

Table 4. Run time analysis.

Methods	Iterations				
	20	40	60	80	100
ALBAE [21]	53.8	51.4	52.9	50.1	49.3
MLP [26]	61.8	63.8	60.2	62.4	59.3
SVM [27]	59.3	56.1	58.5	57.9	55.6
ELM [28]	66.7	62.9	65.3	64.7	61.2
Proposed IGNN-GAO	51.2	49.2	51.8	49.7	47.2

4.6. Segmentation analysis

The segmentation analysis of different algorithms in terms of their respective accuracy is shown in the Table 5 below. It can be seen clearly that the accuracy of segmentation of the MEM algorithm is better than the other state-of-the-art segmentation methods, being considered respectively. Hence, it can be demonstrated that the proposed MEM method of segmentation is better in segmenting the lung cancer than the other methods, respectively.

Table 5. Segmentation analysis.

Methods	Segmentation accuracy
IGJO [2]	95.8
MDE [4]	94.2
mRSA [6]	97.1
COVIDOA+HHOA [8]	98.4
LCWOA [10]	96.7
DREFC [17]	96.4
SV-net [29]	97.1
Self-supervised DL method [30]	95.2
LCP-CNN [31]	98.2
Proposed MEM	98.9

5. Conclusions

To expedite the critical process of identifying lung cancer and reduce the stress on pathologists, deep learning algorithms were used. Examining cancer histology slides has improved the efficiency of these techniques. The common benchmark dataset was where the data were initially acquired. Additionally, the acquired images were pre-processed using the Gabor filter technique. These pre-processed images were segmented via the MEM algorithm technique. The characteristics were then retrieved from these segmented images using the HOG technique. The IGNN was used to classify lung cancer, and the GAO method was used to optimize the parameters of the GNN in order to maximize accuracy as the main objective function. The final output of this IGNN categorized lung cancer as normal, adenocarcinoma and squamous cell carcinoma. The simulation results showed that the new approach was superior to existing methods when compared to several performance measures. In the future, the proposed model can be extended to various concerns such as prediction of lung cancer at an early stage and it can be determined using some enhanced form of hybrid deep learning algorithms being tuned by some form of novel nature-inspired metaheuristic optimization algorithms.

Use of AI tools declaration

The authors declare they have not used Artificial Intelligence (AI) tools in the creation of this article.

Acknowledgments

We would like to thank our institutions for their support related to infrastructure. No funds gathered by any of the sources.

Conflict of interest

The authors declare there is no conflict of interest.

References

1. A. Masood, P. Yang, B. Sheng, H. Li, P. Li, J. Qin, et al., Cloud-based automated clinical decision support system for detection and diagnosis of lung cancer in chest CT, *IEEE J. Transl. Eng. Health Med.*, **8** (2020), 1–13, 2020. https://doi.org/10.1109/JTEHM.2019.2955458
2. E. H. Houssein, D. A. Abdelkareem, M. M. Emam, M. A. Hameed, M. Younan, An efficient image segmentation method for skin cancer imaging using improved golden jackal optimization algorithm, *Comput. Biol. Med.*, **149** (2022), 106075. https://doi.org/10.1016/j.compbiomed.2022.106075
3. O. Ayyildiz, Z. Aydin, B. Yilmaz, S. Karaçavu, K. Senkaya, S. Içer, et al., Lung cancer subtype differentiation from positron emission tomography images, *Turk. J. Electr. Eng. Comput. Sci.*, **28** (2020), 262–274. https://doi.org/10.3906/elk-1810-154
4. L. Ren, D. Zhao, X. Zhao, W. Chen, L. Li, T. Wu, et al., Multi-level thresholding segmentation for pathological images: Optimal performance design of a new modified differential evolution, *Comput. Biol. Med.*, **148** (2022), 105910. https://doi.org/10.1016/j.compbiomed.2022.105910
5. C. Zappa, S. A. Mousa, Non-small cell lung cancer: Current treatment and future advances, *Transl. Lung Cancer Res.*, **5** (2016), 288–300. https://doi.org/10.21037/tlcr.2016.06.07
6. M. M. Emam, E. H. Houssein, R. M. Ghoniem, A modified reptile search algorithm for global optimization and image segmentation: Case study brain MRI images, *Comput. Biol. Med.*, **152** (2023), 106404. https://doi.org/10.1016/j.compbiomed.2022.106404
7. V. K. Anagnostou, A. T. Dimou, T. Botsis, E. J. Killiam, M. D. Gustavson, R. J. Homer, et al., Molecular classification of nonsmall cell lung cancer using a 4-protein quantitative assay, *Cancer*, **118** (2012), 1607–1618. https://doi.org/10.1002/cncr.26450
8. K. M. Hosny, A. M. Khalid, H. M. Hamza, S. Mirjalili, Multilevel segmentation of 2D and volumetric medical images using hybrid Coronavirus Optimization Algorithm, *Comput. Biol. Med.*, **150** (2022), 106003. https://doi.org/10.1016/j.compbiomed.2022.106003
9. F. Ciompi, K. Chung, S. J. van Riel, A. A. A. Setio, P. K. Gerke, C. Jacobs, et al., Towards automatic pulmonary nodule management in lung cancer screening with deep learning, *Sci. Rep.*, **7** (2017), 1–11. https://doi.org/10.1038/srep46479
10. W. Zhu, L. Liu, F. Kuang, L. Li, S. Xu, Y. Liang, An efficient multi-threshold image segmentation for skin cancer using boosting whale optimizer, *Comput. Biol. Med.*, **151** (2022), 106227. https://doi.org/10.1016/j.compbiomed.2022.106227
11. J. J. Chabon, E. G. Hamilton, D. M. Kurtz, M. S. Esfahani, E. J. Moding, H. Stehr, et al., Integrating genomic features for non-invasive early lung cancer detection, *Nature*, **580** (2020), 245–251. https://doi.org/10.1038/s41586-020-2140-0
12. A. Masood, B. Sheng, P. Yang, P. Li, D. D. Feng, Automated decision support system for lung cancer detection and classification via enhanced RFCN with multilayer fusion RPN, *IEEE Trans. Ind. Inf.*, **16** (2020), 7791–7801. https://doi.org/10.1109/TII.2020.2972918
13. M. Bicakci, O. Ayyildiz, Z. Aydin, A. Basturk, S. Karacavus, B. Yilmaz, Metabolic imaging based sub-classification of lung cancer, *IEEE Access*, **8** (2020), 218470–218476. https://doi.org/10.1109/ACCESS.2020.3040155
14. Y. Chen, Y. Wang, F. Hu, L. Feng, T. Zhou, C. Zheng, LDNNET: Towards robust classification of lung nodule and cancer using lung dense neural network, *IEEE Access*, **9** (2021), 50301–50320. http://doi.org/10.1109/ACCESS.2021.3068896

15. M. Li, X. Ma, C. Chen, Y. Yuan, S. Zhang, Z. Yan, et al., Research on the auxiliary classification and diagnosis of lung cancer subtypes based on histopathological images, *IEEE Access*, **9** (2021), 53687–53707. https://doi.org/10.1109/ACCESS.2021.3071057
16. E. A. Siddiqui, V. Chaurasia, M. Shandilya, Detection and classification of lung cancer computed tomography images using a novel improved deep belief network with Gabor filters, *Chemom. Intell. Lab. Syst.*, **235** (2023), 104763. https://doi.org/10.1016/j.chemolab.2023.104763
17. A. K. Ajai, A. Anitha, Clustering based lung lobe segmentation and optimization-based lung cancer classification using CT images, *Biomed. Signal Process. Control*, **78** (2022), 103986. https://doi.org/10.1016/j.bspc.2022.103986
18. A. R. Bushara, R. S. Vinod Kumar, S. S. Kumar, LCD-capsule network for the detection and classification of lung cancer on computed tomography images, *Multimedia Tools Appl.*, **2023** (2023), 1–20. https://doi.org/10.1007/s11042-023-14893-1
19. D. S. Manoharan, A. Sathesh, Improved version of graph-cut algorithm for CT images of lung cancer with clinical property condition, *J. Artif. Intell.*, **2** (2020), 201–206. https://doi.org/10.36548/jaicn.2020.4.002
20. A. Alsadoon, G. Al-Naymat, A. H. Osman, B. Alsinglawi, M. Maabreh, M. R. Islam, DFCV: A framework for evaluation deep learning in early detection and classification of lung cancer, *Multimedia Tools Appl.*, **93** (2023), 1–44. https://doi.org/10.1007/s11042-023-15238-8
21. M. Braveen, S. Nachiyappan, R. Seetha, K. Anusha, A. Ahilan, A. Prasanth, et al., ALBAE feature extraction-based lung pneumonia and cancer classification, *Soft Comput.*, **155** (2023), 1–14. https://doi.org/10.1007/s00500-023-08453-w
22. Y. Chen, C. Liu, W. Huang, S. Cheng, R. Arcucci, Z. Xiong, Generative text-guided 3D vision-language pretraining for unified medical image segmentation, *arXiv preprint*, (2023), arXiv:2306.04811. https://doi.org/10.48550/arXiv.2306.04811
23. Z. Qin, H. Yi, Q. Lao, K. Li, Medical image understanding with pre-trained vision language models: A comprehensive study, *arXiv preprint*, (2022), arXiv:2209.15517. https://doi.org/10.48550/arXiv.2209.15517
24. Z. Wan, C. Liu, M. Zhang, J. Fu, B. Wang, S. Cheng, et al., Med-UniC: Unifying cross-lingual medical vision-language pre-training by diminishing bias, *arXiv preprint*, (2023), arXiv:2305.19894. https://doi.org/10.48550/arXiv.2305.19894
25. M. Lavanya, P. Muthu Kannan, Lung cancer segmentation and diagnosis of lung cancer staging using MEM (modified expectation maximization) algorithm and artificial neural network fuzzy inference system (ANFIS), *Biomed. Res.*, **29** (2018), 2919–2924. https://doi.org/10.4066/biomedicalresearch.29-18-740
26. F. Mirzakhani, Detection of lung cancer using multilayer perceptron neural network, *Med. Technol. J.*, **1** (2017), 109. http://doi.org/10.26415/2572-004X-vol1iss4p109
27. N. Shukla, A. Narayane, A. Nigade, K. Yadav, H. Mhaske, Lung cancer detection and classification using Support Vector Machine, *Int. J. Adv. Trends Comput. Sci. Eng.*, **4** (2015), 14983–14986. http://doi.org/10.18535/Ijecs/v4i11.20
28. M. Grace John, S. Baskar, Extreme learning machine algorithm-based model for lung cancer classification from histopathological real-time images, *Comput. Intell.*, **2023** (2023). https://doi.org/10.1111/coin.12576

29. F. Zhu, Z. Gao, C. Zhao, Z. Zhu, J. Tang, Y. Liu, et al., Semantic segmentation using deep learning to extract total extraocular muscles and optic nerve from orbital computed tomography images, *Optik*, **244** (2021), 167551. https://doi.org/10.1016/j.ijleo.2021.167551
30. Y. Song, J. Liu, X. Liu, J. Tang, COVID-19 infection segmentation and severity assessment using a self-supervised learning approach, *Diagnostics*, **12** (2022), 1805. https://doi.org/10.3390/diagnostics12081805
31. M. A. Heuvelmans, P. M. A. van Ooijen, S. Ather, C. F. Silva, D. Han, C. P. Heussel, et al., Lung cancer prediction by deep learning to identify benign lung nodules, *Lung Cancer*, **154** (2021), 1–4. https://doi.org/10.1016/j.lungcan.2021.01.027

AIMS Press